Across-Track Tilt Concept for Sun Glint Mitigation in Future Earth-Observing Missions

Saeed Arab, Christopher J. Crawford, Benjamin Page, Kevin R. Turpie, Peter Gege, David R. Thompson, *Senior Member, IEEE*, and Kelly M. A. Luis

***Abstract*—Sun glint is a major limitation for spaceborne optical remote sensing of aquatic environments, particularly in tropical and subtropical regions. By dominating the at-sensor radiance, sun glint complicates atmospheric correction and reduces the quality of aquatic reflectance products derived across Earth observation missions. This study presents a machine learning framework to quantify sun glint probability and evaluates the across-track tilt observational concept as a potential sun glint mitigation approach for satellite remote sensing missions. More than 14,000 cloud-free Landsat 8 and 9 scenes were analyzed to quantify glint occurrence as a function of sun-sensor geometry, latitude, and season. Logistic regression and machine learning models identified solar zenith angle (SZA), wind speed, and viewing zenith angle (VZA) as the primary predictors of sun glint probability, achieving > 98% classification accuracy. Sun glint contamination was found to be negligible for SZA > 40° but frequent at SZA < 35°, particularly in forward-scattering geometries. Introducing a 3° across-track westward tilt reduces the proportion of glint-contaminated pixels by ~21% in tropical and subtropical regions, while larger tilts of 6°, 9°, and 12° yield reductions of 43%, 59%, and 74%, respectively. These findings underscore the value of incorporating glint mitigation strategies in future Earth observing mission designs. A modest across-track tilt, combined with post-acquisition glint detection and correction, offers a practical pathway to increasing the availability of high-quality aquatic observations for monitoring inland and coastal water quality and ecosystems.**

***Index Terms*—Aquatic remote sensing, Landsat, sun glint, sun-sensor geometry.**

I. Introduction

U.S. Geological Survey (USGS) and National Aeronautics and Space Administration (NASA) jointly operate the Landsat program, which has been providing global medium-resolution multispectral observations of the Earth's surface for more than five decades [1], [2]. Although Landsat missions were originally developed for monitoring terrestrial environments [3], advances in Operational Land Imager (OLI) onboard Landsat 8 (since 2013) and 9 (since 2021) have enabled reliable visible-to-shortwave infrared (VSWIR) observations of inland and coastal aquatic ecosystems [4], [5]. Improvements in signal-to-noise ratio (SNR), radiometric resolution, spectral sampling, and calibration have enabled high-fidelity observations and made these missions applicable to water quality and ecosystem studies [6], [7], [8]. These observational capabilities have supported a broad range of aquatic applications, including retrieval of nearshore bathymetry for coastal monitoring in shallow waters [9], detection and tracking of algal blooms in drinking-water reservoirs [10], and estimation of key water-quality parameters such as chlorophyll-a and turbidity in riverine systems [11]. Collectively, these advances have expanded the role of Landsat in the aquatic community, enabling consistent, moderate resolution, and long-term observations that support coastal management, inland water monitoring, and water-quality assessment at regional to global scales.

One of the major challenges in spaceborne remote sensing of water bodies is sun glint, the specular reflection of sunlight from the water surface [12]. Sun glint generally occurs when the sensor viewing angle aligns with the angle of direct solar reflection [13] and is further broadened by water surface roughness and atmospheric scattering, often contaminating large areas of imagery. Because aquatic observations rely on photons backscattered from within the water column, the surface-reflected glint signal adds noise that can overwhelm the subtle water-leaving radiance needed to characterize water quality, productivity, and benthic composition [14]. Sun glint is especially problematic in equatorial latitudes, where most coral reefs are located, limiting the utility of aquatic imagery for coastal ecosystem studies [15]. Atmospheric correction also becomes highly uncertain under sun glint conditions [7], [12]. In practice, sun glint must typically be avoided or corrected for in most aquatic science applications, except when measuring the water surface roughness [16].

Although several ocean color missions have adopted along- and across-track tilt observational configurations to avoid high-intensity sun glint near the subsolar point, land-imaging missions such as Landsat have historically operated in nadir-viewing mode optimized for terrestrial observations. Nevertheless, as demonstrated by current Landsat missions, the land-imaging missions also provide data that support monitoring and analysis of inland, estuarine, and coastal aquatic ecosystems. Future land-imaging missions are expected to place greater emphasis on aquatic applications. The 2018 National Academies Decadal Survey identified aquatic ecology as a priority science area [17], and user needs

Received 11 December 2025; revised 30 April 2026; accepted 25 June 2026. Date of publication 3 July 2026; date of current version 16 July 2026. This work was supported in part by U.S. Geological Survey (USGS) Core Science Systems National Land Imaging Program through the Phase 2 Imaging Spectroscopy Research and the Development Project under Grant GX23ED00TYG and in part by USGS Core Science Systems National Land Imaging Program through Land Satellites Data System Research and Development Project under Grant GX26ED00EDK1A00. A portion of this research was carried out at the Jet Propulsion Laboratory, California Institute of Technology, under a contract with the National Aeronautics and Space Administration (80NM0018D0004). *(Corresponding author: Saeed Arab.)*

Saeed Arab is with KBR, U.S. Geological Survey (USGS), Earth Resources Observation and Science (EROS) Center, Sioux Falls, SD 57198 USA (e-mail: sarab@contractor.usgs.gov).

Christopher J. Crawford is with USGS, EROS Center, Sioux Falls, SD 57198 USA (e-mail: cjcrawford@usgs.gov).

Benjamin Page is with ESTS, USGS, EROS Center, Sioux Falls, SD 57198, USA (e-mail: bpage@contractor.usgs.gov).

Kevin R. Turpie is with the University of Maryland, Baltimore County, Baltimore, MD 21250 USA (e-mail: kturpie@umbc.edu).

Peter Gege is with the Remote Sensing Technology Institute, German Aerospace Center (DLR), 82234 Oberpfaffenhofen, Germany (e-mail: Peter.Gege@dlr.de).

David R. Thompson and Kelly M. A. Luis are with the Jet Propulsion Laboratory, California Institute of Technology, Pasadena, CA 91109 USA (e-mail: david.r.thompson@jpl.nasa.gov; kelly.m.luis@jpl.nasa.gov).

Digital Object Identifier 10.1109/TGRS.2026.3709997

© 2026 The Authors. This work is licensed under a Creative Commons Attribution 4.0 License.
For more information, see https://creativecommons.org/licenses/by/4.0/

assessment for future Landsat missions highlighted aquatic monitoring as a key requirement [18]. The planned Landsat 10 mission concept is currently in formulation and will offer improved spectral sampling to support aquatic remote sensing science, among other emerging science applications [2]. Five new spectral bands centered at 600, 620, 650, 705, and 740 nm will improve Landsat 10 observational capability to measure colored dissolved organic matter (CDOM) [19], [20], [21], suspended solids and water clarity/turbidity [22], [23], chlorophyll-a concentration [24], [25], floating algal blooms [26], and the presence of cyanobacteria within harmful algae [27], [28], [29], [30], [31], [32], [33]. Similarly, European Space Agency (ESA) Sentinel-2 Next Generation is planned to launch in mid-2030s and will evolve and extend Sentinel-2 Multispectral Instrument (MSI) global measurements of coastal and inland water bodies [34]. NASA Explorer for Artemis Geology Lunar and Earth (EAGLE)-VSWIR was conceptualized to acquire medium-resolution imaging spectroscopy data over warm water coral reefs, archipelagic waters, marginal seas, and global islands [35], [36]. Collectively, land-observing missions like these will expand the capabilities to monitor inland, estuarine, and coastal water ecosystems. Achieving this potential, particularly at tropical and subtropical latitudes, will require strategies to minimize the sun glint contamination.

This study reviews the challenges of sun glint in optical remote sensing of aquatic targets, leverages data from Landsat 8 and 9 OLI observations to characterize sun glint occurrence, and evaluates the applicability of across-track tilt observational configuration as a mitigation strategy for future land-imaging missions. While tilt strategies have been explored for ocean-color sensors, this work provides, to the best of our knowledge, the first systematic, observation-based assessment of sun glint mitigation geometry for medium-resolution land-imaging platforms, using Landsat as a representative global survey system. The main contributions of this work are: 1) characterization of sun glint occurrence as a function of solar illumination, viewing geometry, and wind conditions using multiyear Landsat 8 and 9 observations; 2) development and evaluation of statistical models to predict sun glint probability under varying acquisition geometries; and 3) quantification of the reduction in sun glint contamination achievable under varying across-track tilt scenarios. In contrast to existing approaches on ocean-color missions that reduce sun glint but can compromise geometric fidelity, revisit consistency, or terrestrial measurement requirements, the proposed analysis evaluates mitigation strategies within the operational constraints of global medium-resolution land-imaging systems. By explicitly considering tradeoffs between aquatic data quality and terrestrial imaging requirements, this work advances the discussion on sun glint mitigation for derived aquatic reflectance and water quality products and provides guidance for optimizing observational strategies in upcoming missions to ensure consistent, high-quality aquatic data.

II. Background

The water surface specularly reflects the solar beam into the sensor's field of view (FOV), producing glint in the image data [37], [38]. Glint may arise from reflection of direct solar irradiance (sun glint) or from diffuse irradiance scattered by the atmosphere (sky glint) [39]. The intensity of glint depends on sun-sensor geometry and water surface roughness, which is largely governed by wind speed and direction at the air–water interface [16], [40]. For rougher water surfaces, the angular extent of sun glint expands, affecting larger portions of the observed imagery.

The at-sensor radiance (L_T) measured over water consists of multiple components, including path radiance due to single and multiple scattering by atmospheric aerosol particles (L_A) and Rayleigh scattering by atmospheric gases (L_R), sun glint (L_g^{TOA}), surface-reflected sky radiance (sky glint) (L_{sky}^{TOA}), reflection of whitecaps (L_{wc}^{TOA}), and water-leaving radiance (L_w^{TOA}) and can be expressed as follows [41]:

$$L_T = L_R + L_A + L_g^{TOA} + L_{sky}^{TOA} + L_{wc}^{TOA} + L_w^{TOA} \quad (1)$$

The superscript "TOA" in (1) indicates the portion of surface-reflected or water-leaving radiance that reaches the top of atmosphere (TOA). Radiative transfer models are applied to characterize interactions of light with atmospheric molecules and particles and to estimate the water-leaving radiance (L_w), which carries information about surface water and benthic features. Although accurate retrieval of L_w requires accounting for all terms in (1) through atmospheric correction, the present study is concerned primarily with the intensity (the presence or absence) of sun glint. A full quantitative characterization of sun glint radiance is beyond the scope of this work.

In the presence of sun glint, estimating apparent optical properties such as water-leaving reflectance is subject to high uncertainty and is sometimes impossible [7], [40]. Therefore, areas with high sun glint probability are typically masked as having too poor of quality for conventional science algorithms during atmospheric correction. For example, the Medium Resolution Imaging Spectrometer (MERIS; 2002–2102) Ground Segment (MEGS) data processing prototype and the NASA level 2 generator (l2gen) code both flag and mask out sun glint pixels during atmospheric correction [42]. It is also a common practice to exclude sun glint pixels from the analysis in aquatic remote sensing studies [43], [44], [45], [46], [47], [48].

Several ocean color imaging missions have incorporated tilt maneuvers to mitigate sun glint during acquisition. The NASA Sea-Viewing Wide Field-of-view Sensor (SeaWiFS; 1997–2010) used a scanner tilt mechanism to orient the instrument to +20°, 0°, and −20° in the along-track direction to avoid sun glint from the sea surface [49]. The Ocean Color Instrument (OCI) onboard the NASA Plankton, Aerosol, Cloud, Ocean Ecosystem (PACE; since 2024) mission performs the same along-track tilt maneuver every orbit at approximately the subsolar point, orienting ~20° north in the northern hemisphere and ~20° south in the southern hemisphere to avoid sun glint reflected off the ocean [50]. The Sentinel-3 Ocean and Land Colour Imager (OLCI; since 2016) uses a fixed 12.6° across-track westward tilt to minimize sun glint [51].

Orbit design can also influence sun glint probability. For sun-synchronous missions, the sun glint can be partially mitigated using earlier in the morning or later in the afternoon

Equatorial Crossing Time (ECT) orbits. The solar zenith angles (SZAs) are at a minimum around noon (11:30 A.M. to 12:30 P.M.) ECT, maximizing the sun glint probability [52]. Instruments with sufficient tilt from the subsolar point can still acquire good quality data even with a noon ECT, as demonstrated by SeaWiFS [53]. Most sun-synchronous Earth observation missions targeting terrestrial surfaces instead of ocean color orbit between 10 and 11 A.M. ECT in descending (Terra MODIS, MERIS, Landsat series, Sentinel-2 MSI, EnMAP, PRISMA, planned CHIME) or 1–2 P.M. ECT in ascending node (Aqua MODIS and VIIRS). Optimizing observations for both terrestrial and aquatic science involves tradeoffs among FOV, SNR, the desire to maximize cloud-free observations, and specific biophysical process targets such as evapotranspiration. For Landsat missions, the ECT has historically been constrained to between 9:45 and 10:15 A.M. Continuity of land surface measurements is a core principle for the five-decade Landsat program, and thus, sun glint is not considered a primary modulator for mission observational ECT design. The Landsat 10 ECT has been defined by NASA and USGS at 10:10 A.M., ±5 min of margin [2].

Sun glint contamination can be corrected post-acquisition by estimating the glint contribution to at-sensor radiance and subtracting the contribution from the total signal [54], [55]. Conventional glint detection algorithms are based on the geometry of sun glint. One of the original sun glint detection algorithms applied by Wang and Bailey [53] is based on the expression [16] for the reflection coefficient of a rough water surface. In this approach, sun glint radiance is computed based on the solar–viewing geometries and a relationship between analytical wind speed and wave slope distribution. The geometry-based sun glint detection techniques rely on the probability distribution of water surface slope as a function of surface wind speed and direction, which is more applicable to open ocean and coarser ground sampling distance (≥ 100 m), where the pixel size is comparable to average known or predicted wind fields. At higher spatial resolutions (< 10 m), pixel size is too small to resolve local wind fields and begins to resolve the systematic effects of wave swells. Instead, coastal imagery sun glint correction is based on the measured radiance in the near infrared (NIR) and shortwave infrared (SWIR) wavelengths. Given that clear, moderately deep water absorbs more than 95% of downwelling irradiance in these wavelengths [56], any remaining water-leaving radiance after the atmospheric correction could be attributed to sun glint [57]. This approach has limitations over turbid or shallow water, where water-leaving radiance in the NIR is nonzero. This approach can also fail in conditions with significant aerosol loads that increase the NIR signal. For a comprehensive review of the geometry based and infrared-based sun glint detection algorithms, refer to [58] and [59]. More recent approaches explicitly model the spectral dependence and intensity of glint by accounting for direct and diffuse irradiance [39], [60] and incorporating wavelength-dependent refractive index at the air–water interface [14], [55]. For imaging spectroscopy data, optimal estimation (OE) methods have been used to simultaneously model atmospheric effects and correct for both sun and sky glint [61].

Despite these advances, avoiding sun glint during image acquisition by selecting proper time and place of acquisition remains a more effective strategy [58]. However, sensors with tilt capabilities can still experience residual glint radiance reaching the sensor, e.g., near the edges of the effective glint area [41]. Therefore, for missions that include aquatic observations, incorporating a systematic sun glint avoidance strategy together with postacquisition glint detection and correction represents a robust approach for ensuring high-quality aquatic observations.

III. Data and Methods

A. Landsat 8 and 9 Data

To evaluate sun-sensor geometry dependency of sun glint, we used the Landsat 8 and 9 provisional Level 2 Aquatic Reflectance product [62]. The provisional Aquatic Reflectance data product was obtained from the USGS EROS Science Processing Architecture (ESPA) interface (https://espa.cr.usgs.gov). This product is generated by applying the NASA Ocean Biology Processing Group (OBPG) SeaWiFS Data Analysis System (SeaDAS) on Landsat 8/9 OLI Collection 2 Level 1 (L1) TOA reflectance [63], [64]. SeaDAS detects sun glint using the model developed by Cox and Munk [16], which provides a probability distribution function for surface facets being oriented in the specular direction, parameterized as a function of wind speed [65]. The spectral glint radiance is expressed as follows:

$$L_g(\lambda) = \frac{\rho T_0(\lambda, \theta_s) F_0(\lambda) P_W(\theta_v, \phi_v, \theta_s, \phi_s, W)}{4 \cos\theta_v \cos^4\theta_s} \quad (2)$$

where L_g is spectral glint radiance, ρ is the Fresnel reflectivity, T_0 is the atmospheric downward transmittance, F_0 is the extraterrestrial solar irradiance, and P_w is the probability of sun glint in wind speed W. The wind speed in SeaDAS processing of Landsat data is derived from the hourly 50-km zonal and meridional wind fields in GEOS-IT reanalysis, using the time step closest to the Landsat overpass time and resampled to Landsat pixel resolution [66]. The argument angles (θ_v, ϕ_v) describe sensor viewing direction and (θ_s, ϕ_s) describe sun position in this expression. Image pixels with a glint radiance $L_g(865) > 0.005F_0(865)$ are flagged as high sun glint in SeaDAS Level-2 quality flags [67]. This high-sun glint flag was used for subsequent characterization of glint occurrence as a function of solar illumination and viewing geometry. Although in reality almost all pixels contain some degree of sun glint, for simplicity, we refer to pixels as "glint-contaminated" (Glint = 1) and "glint-free" (Glint = 0) depending on whether the high sun glint flag is set. SeaDAS also provides a moderate sun glint contamination flag which is not used in this analysis.

We analyzed 14971 clear-sky (< 5% cloud cover) Landsat 8 and 9 scenes acquired between April 2013 and December 2024 across 65°S–70°N latitudes. The dataset included 12,924 coastal/open-ocean and 2,047 inland scenes. To ensure sufficient surface water coverage, scene selection was performed by intersecting global land–water masks with World Reference System-2 (WRS-2) path/row footprints to estimate water fraction. Path/rows containing at least 15% coastal/open-ocean water or at least 5% inland water were retained to ensure representative sampling of both coastal and inland aquatic environments (see Fig. 1). A stratified random sampling based on scene-center SZA was then applied to ensure the balanced representation of solar illumination

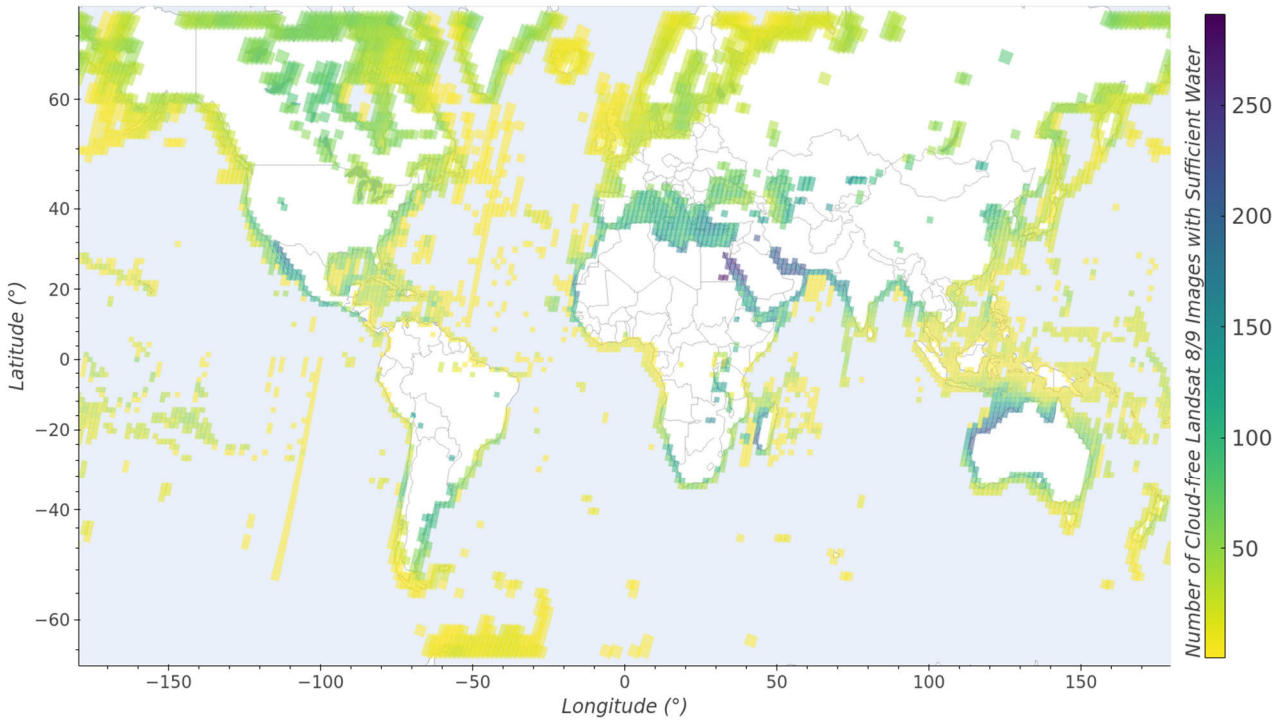


Fig. 1. Geographic distribution of the cloud-free Landsat 8 and Landsat 9 scenes used for sun glint characterization. Coastal/open-ocean WRS-2 path/row locations with ≥ 15% water pixels and inland scenes with ≥ 5% water pixels were retained.

conditions. At the pixel level, the quality assessment layer derived from FMask [68] was used to identify clear water pixels for statistical analyses. In total, ~7 million unique cloud-free water pixels were randomly selected across the study scenes, of which 14.8% were classified as sun glint by SeaDAS.

B. Sun Glint Predictor Variables

Geographic latitude (Lat), sun-sensor geometries, scattering angle (SCA), and acquisition day-of-year (DOY) were analyzed as primary variables to characterize the seasonal and spatial variability of the sun glint. The relative azimuth angle (RAA; $\Delta\phi$) and directional slope facets (ζ_x and ζ_y) were computed using the sun-sensor geometry, given as follows [69]:

$$\Delta\phi = min \begin{cases} |\phi_s - \phi_v| \\ 360^\circ - |\phi_s - \phi_v| \end{cases} \tag{3}$$

$$\zeta_x = -\left(\sin\theta_s + \sin\theta_v \cos\Delta\phi\right) / \left(\cos\theta_s + \cos\theta_v\right) \tag{4}$$

$$\zeta_y = -\left(\sin\theta_v \sin\Delta\phi\right) / \left(\cos\theta_s + \cos\theta_v\right) \tag{5}$$

where ϕ_s is the solar azimuth angle (SAA), θ_s is the SZA, ϕ_v is the viewing azimuth angle (VAA), and θ_v is the viewing zenith angle (VZA). Fig. 2 shows the scatterplot matrix of sun glint classification as a function of these predictor variables. The lower triangle displays the density scatterplots for each variable pair, and the upper triangle reports the corresponding coefficient of determination (R^2) for glint-contaminated (Glint = 1), glint-free (Glint = 0), and all pixels. The diagonal represents the density histogram of the pixels, with the density violin plots along the top row. As expected, for Landsat 8/9 with ~10:00 A.M. ± 15 min ECT and nadir-viewing geometry, sun glint is more probable at low SZA, where the instrument is pointed toward the subsolar point. Sun glint is restricted to SZA < 40°, with an interquartile range of 23.8°–28.6°. The VZA distribution of glint-contaminated pixels is skewed toward the forward-viewing portion of the Landsat scenes (eastern half of image in descending node) illustrated using positive VZA values. The bimodal distribution of SAA and latitude represents the data from northern and southern hemispheres. The limited number of data points from the tropical and subtropical regions (15°S < latitude < 15°N) is due to persistent cloud cover and filtering/masking applied during scene and pixel selection. The strong collinearity between SZA, SCA, and slope facet in the solar direction (ζ_x) indicates that these variables must be selected carefully when developing sun glint characterization models (refer to Section IV-A).

1) Viewing Geometry: Fig. 3 illustrates the sun glint frequency as a function of SZA and VZA geometries. The total number of pixels and glint percentage histogram is illustrated using 5° SZA classes and 1° VZA bins. The upper row shows the number of pixels classified by glint condition, and the bottom row shows the percentage of glint-contaminated pixels. Although relatively fewer pixels are observed in the 20° ≤ SZA < 25° range, the percentage of glint is substantially higher under these low solar zenith conditions (near the subsolar point), and the glint percent decreases as the SZA class increases. Data for SZA ≥ 45° are not displayed because glint is almost nonexistent beyond SZA ≈ 40°. In each subplot, the glint percent increases from west to east, indicating higher probability in forward scattering views of Landsat imagery. Maximum glint contamination would occur in solar principal plane regions where the SZA ≈ VZA in forward scattering

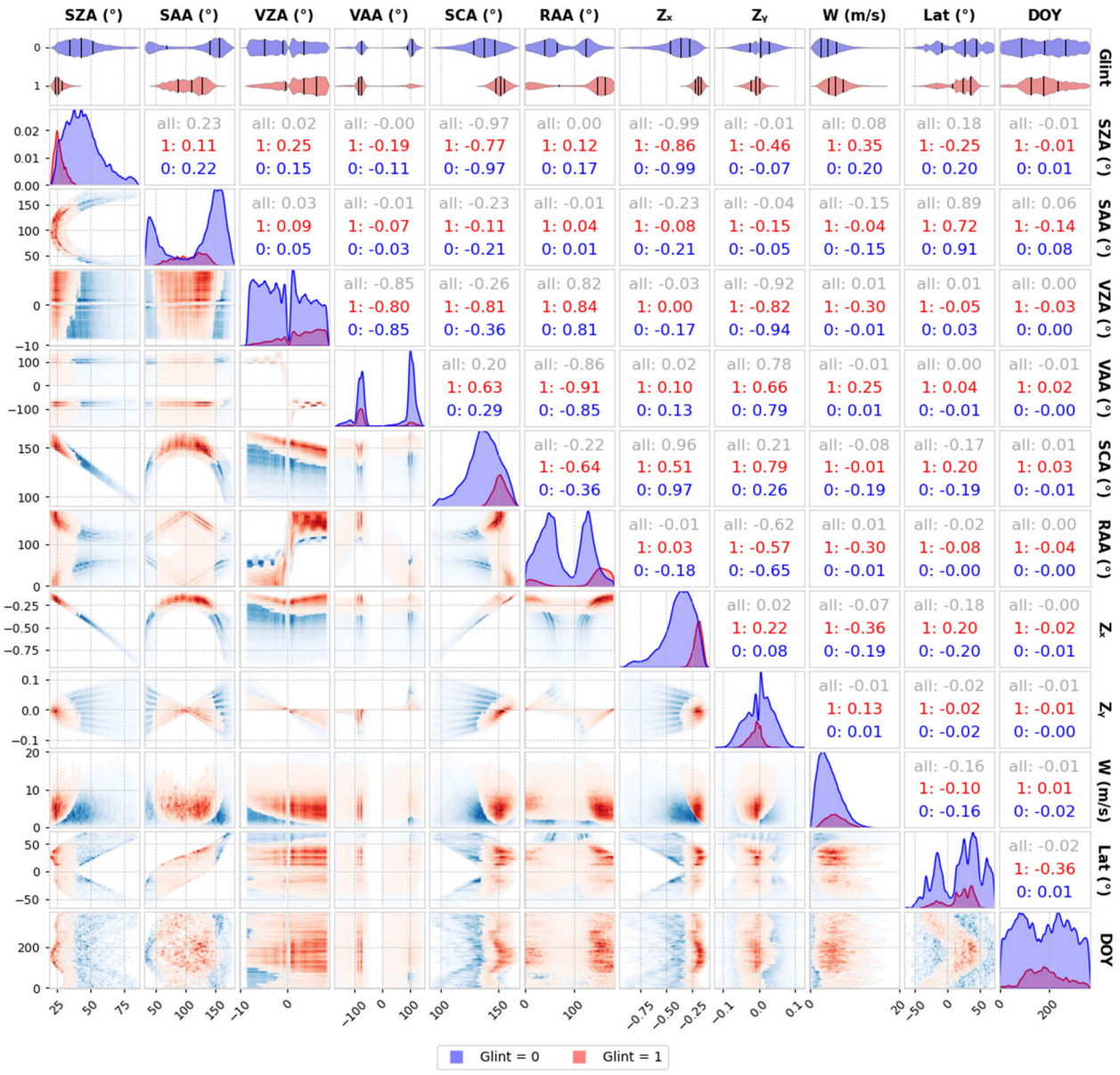


Fig. 2. Scatterplot matrix of observation geometry and conditions for sun glint-contaminated (Glint = 1; red) and glint-free (Glint = 0; blue) pixels. The lower triangle displays the density scatterplots for each variable pair, the upper triangle shows the regression R^2 for all, glint-contaminated, and glint-free pixels, and the diagonal represents the density histogram of the pixels.

view. However, this "hotspot" condition never occurs with relatively narrow FOV and 10:00 A.M. ECT of the Landsat 8/9 missions [70].

The RAA density histogram and scatterplots in Fig. 2 indicate that relative azimuth angles within 45° < RAA < 135° are generally associated with lower sun glint probability, a pattern further illustrated in Fig. 4. Specifically, Fig. 4 shows a polar histogram of the percentage of glint-contaminated pixels as a function of RAA. While the distribution is approximately symmetric about RAA = 90°, the probability of sun glint in Landsat observations is generally higher for RAA > 90° (bottom portion of the half-circle in Fig. 4). This behavior arises because RAA > 90° corresponds to forward-scattering viewing geometry (VZA > 0), which is more prone to sun glint contamination. The strong correlation between RAA and VZA (overall $R^2 = 0.82$) is shown in Fig. 2. A local increase in sun glint probability is observed near RAA ≈ 90°. This feature is attributed to a larger number of wave facet orientations satisfying the specular reflection condition under near-nadir viewing geometry (VZA ≈ 0) and can be traced to the percentage of pixels with relatively high ζ_x value. Inspection of sun glint contamination percentage in Fig. 4 indicates that an RAA of 55°–60° or 115°–120° yields minimum sun glint contamination. This relationship is expected to hold for spaceborne aquatic remote sensing systems with relatively narrow FOV, such as Landsat. The observation that the RAA of 90° is not optimum for sun glint mitigation is consistent with the findings from radiative transfer simulations [71]. Radiative transfer simulations indicate that for field measurements a 90° < RAA < 135° (ideally 135°) combined with VZA of 40° minimizes the sun glint and self-shadowing [71], [72]. The apparent discrepancy between the recommended RAA

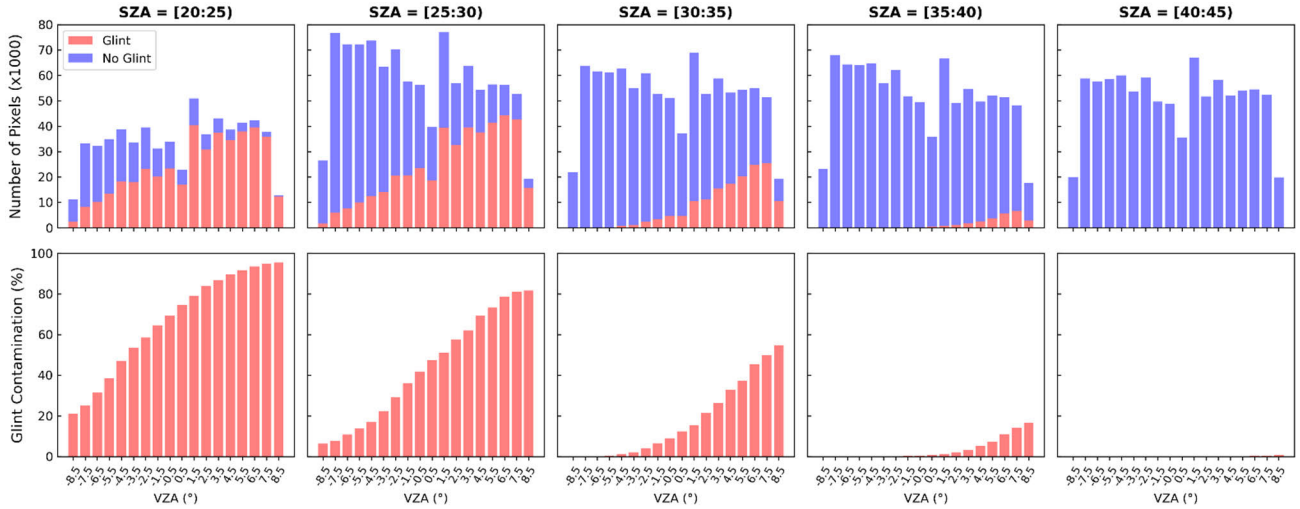


Fig. 3. Total number of observed pixels (top row) and sun glint percentage (bottom row) as a function of solar-viewing zenith geometries. Forward- and backward-looking pixels are represented by positive and negative VZA values, respectively.

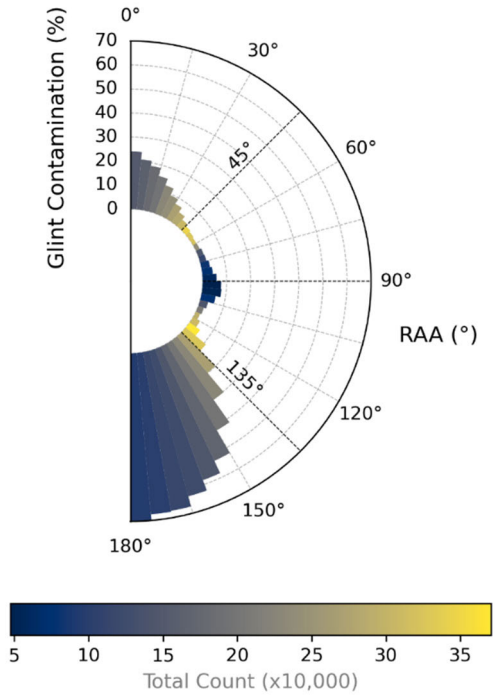


Fig. 4. Semicircular polar histogram showing the percentage of sun glint contaminated pixels as a function of RAA and indicating that an RAA of 90° ± 45° would yield minimum sun glint. The color map represents the total pixel counts per RAA bin.

arises because field instruments typically operate at larger VZAs for practical deployment, while Landsat observations are constrained to relatively small VZAs (−8.3° < VZA < 8.3° for nadir-viewing acquisitions). To ensure consistency between the geometry of satellite observations and coincident in situ measurements, targeting an RAA range of 115°–135° appears to provide a practical compromise for minimizing sun glint contamination in both remotely sensed and field-measured data.

2) Seasonality of Solar Illumination in Sun-Synchronous Orbits: Seasonal variation in glint frequency depends on the solar zenith geometry at the time of the Landsat overpass. Fig. 5 shows the heatmap of the monthly averaged SZA of all Landsat 8 and 9 observations between 2013 and 2025 for March, September, June, and December, representing the spring/autumn equinoxes and summer/winter solstices, respectively. Sun glint is expected to be more frequent between the hemispherical spring and fall equinoxes, when solar zenith is at or near its minimum. Fig. 6 illustrates this seasonal dependency in the studied scenes. Persistently low SZA between the tropics of Cancer and Capricorn throughout the year makes the water bodies between 30°S and 30°N particularly prone to sun glint contamination.

C. Statistical Analysis

This study assesses the importance of predictor variables using random forest (RF) and eXtreme gradient boosting (XGBoost) models. These tree-based ensemble methods were selected due to their strong predictive performance, robustness to multicollinearity, and ability to model nonlinear relationships without extensive feature engineering [73], [74]. In addition, RF and XGBoost provide interpretable measures of variable importance and partial dependence, offering greater transparency compared to more complex approaches, such as neural networks [75]. Feature importance was evaluated with both permutation importance and SHapley Additive exPlanations (SHAP) values to quantify the individual contribution of each variable [76]. We then analyzed interactions among these variables using logistic regression and used a recursive additive modeling approach to identify the optimal predictive model (refer to Section IV-A). All variables were standardized prior to the logistic regression to account for differences in scale.

IV. Results

A. Predictor Variables Importance

The RF and XGBoost models were used to assess the relative importance and contribution of predictor variables

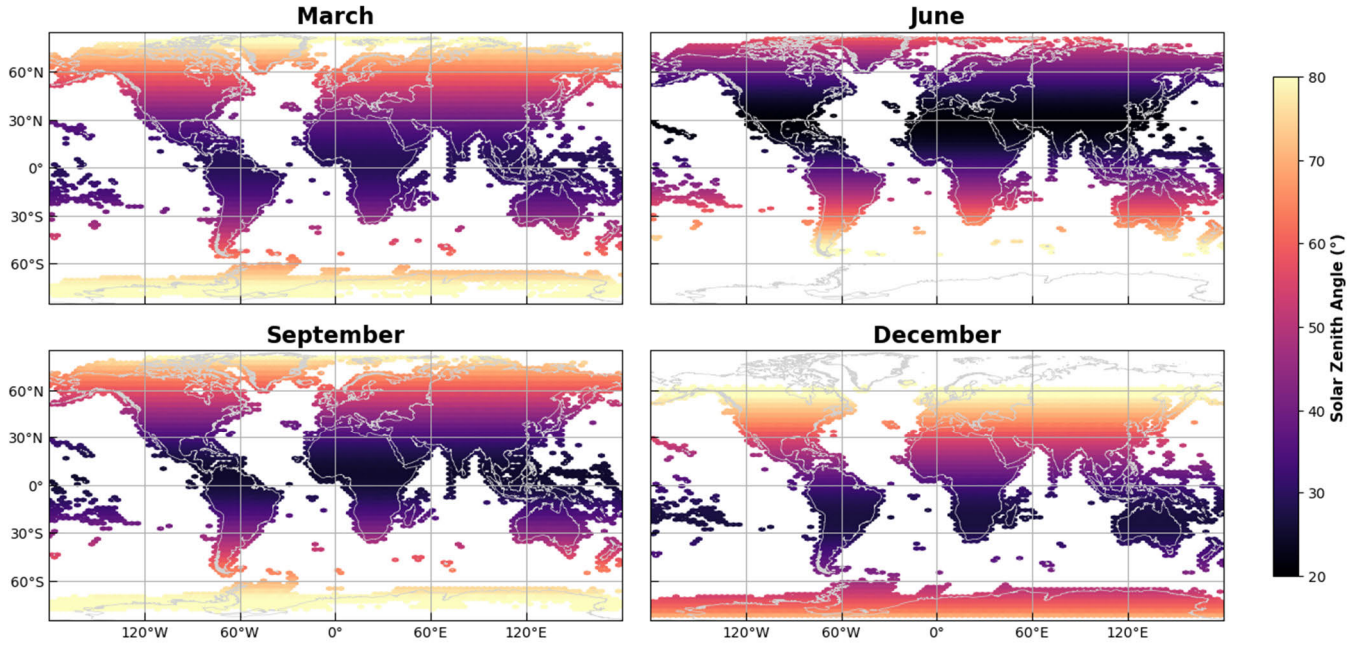


Fig. 5. Latitudinal dependency of SZA for Landsat 8 and 9 data between 2013 and 2025 averaged for (top left) March, (top right) June, (bottom left) September, and (bottom right) December. White color over the land masses indicates that the Landsat data were not collected during that month due to low-illumination conditions.

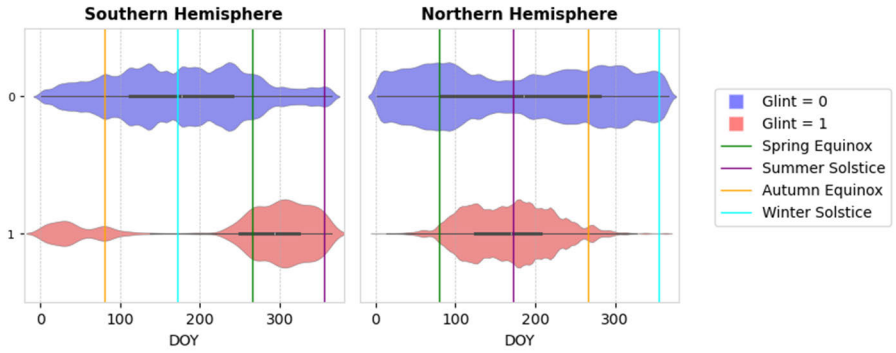


Fig. 6. Violin plots showing the seasonal variation in Landsat sun glint frequency, peaking between the spring and fall equinoxes when SZA is lowest.

for sun glint classification. To address collinearity, SCA was excluded from the variable importance and modeling analyses because of its strong correlation with SZA. In addition, the slope components in the sun and cross-sun directions (ζ_x and ζ_y) were removed because the ζ_x and the combined surface slope ($\arctan((\zeta_x^2 + \zeta_y^2)^{1/2})$) were also strongly correlated with the SZA.

Fig. 7 shows the predictor importance ranking for an XGBoost model trained on 80% of the data and tested on the remaining 20%. The contribution of each variable to the predictive performance of the trained model is expressed using permutation importance scores. The SHAP importance scores indicate how much each feature shifts a prediction from the model's average output while holding all other features fixed. Across both the RF and XGBoost models, SZA, wind speed, and VZA were consistently the dominant predictors; RAA showed moderate importance, and the remaining variables contributed minimally. These patterns are consistent with the physical basis of sun glint, which depends on alignment of solar and viewing geometry, and is modulated by wind-driven surface roughness.

B. Sun Glint Modeling

Permutation importance computed in Section IV-A does not account for interaction effects; therefore, variables that contribute to predictive performance primarily through interactions with other variables may be undervalued. To address this, logistic regression was applied to predict sun glint probability. In the context of low-dimensional data where the number of covariates is small compared wit the sample size, logistic regression is a standard approach for binary classification, especially when the objective extends beyond prediction to include explanation [77].

To develop the logistic regression model, the data were randomly split into training (80%) and testing (20%) subsets. The second-degree polynomial function of predictor variables with interaction terms was defined, and the recursive feature addition approach was used to optimize the tradeoff between

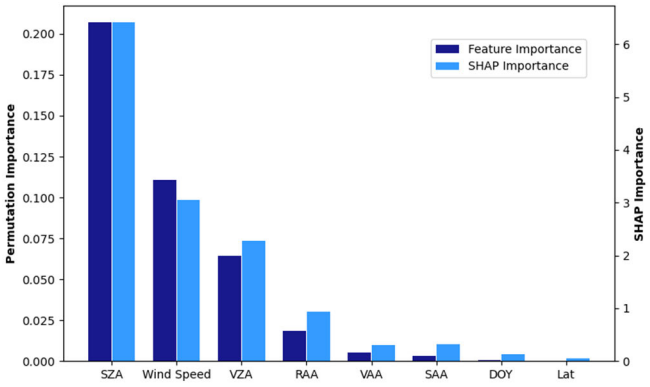


Fig. 7. Permutation and SHAP importance of predictor variables for sun glint classification using the XGBoost model. Permutation importance scores measure the decrease (0–1) in model accuracy when the values of each predictor are randomly shuffled, indicating their relative contribution to predictive performance. SHAP importance scores represent the average magnitude of each feature's contribution (in log-odds units) to model predictions across the dataset. Both methods identify the same relative ranking for the dominant predictors (SZA, wind speed, VZA, and RAA), with minor differences in the ranking of less influential variables (e.g., VAA and SAA).

the bias and variance. At each step, fivefold cross validation was applied, and new term was retained only if it improved the cross-validation score by at least 3%. Equation (6) presents the logistic regression model, with P being the probability of sun glint

$$ln\left(\frac{P}{1-P}\right) = -31.646 - 19.303\ SZA_{std} + 22.903\ W_{std} - 22.546\ SZA_{std} \times W_{std} + 9.102\ VZA_{std}. \quad (6)$$

The subscript "std" in (6) indicates these features were standardized by removing the mean and scaling to unit variance. Specifically, each predictor variable (x^i) was standardized by subtracting its mean (μ) and then dividing by its standard deviation (σ), as shown in (7) [78]. Standardization was necessary because predictors span different orders of magnitude (refer to Fig. 2). In addition, standardization improves the stability of the optimization approach and enhances the interpretability of the model coefficients [79]

$$x^i_{std} = \frac{x^i - \mu}{\sigma}. \quad (7)$$

The predictor variables and their magnitudes in the final model indicate that SZA and wind speed (W) are primary factors in predicting the glint conditions, consistent with results of machine learning models described in Section IV-A. An initial model using only SZA achieved an accuracy of 88.5%. Adding wind speed (W) and interaction term SZA × W increased the accuracy to 92.6%. This improvement is consistent with previous findings that sun glint radiance depends on wind speed [80]. The negative coefficient for SZA confirms that the odds of sun glint decrease with increasing SZA, while positive coefficient of wind speed indicates sun glint is more likely at higher wind speed. Finally, incorporating an additional VZA term further improved the logistic regression model, achieving an accuracy of 98.7% (k = 0.9869) on the 20% test dataset (see Fig. 8). This accuracy can marginally increase up to 99.6% by including other predictor variables and their interaction terms. However, those other predictor variables were not

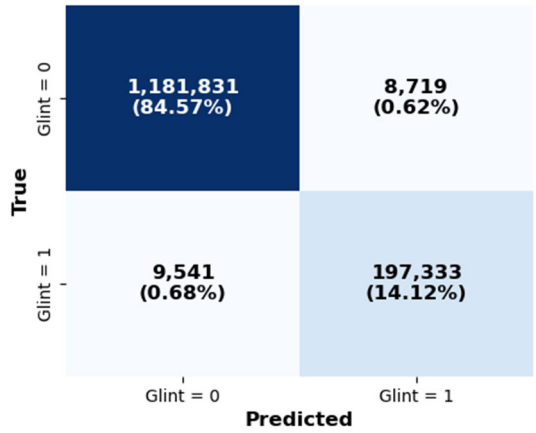


Fig. 8. Confusion matrix for sun glint classification using logistic regression. Diagonal entries indicate the number of correct predictions in the 20% test dataset, with corresponding percentages in parentheses. The sum of the diagonal percentages (98.69%) represents the overall model accuracy.

included in final model to avoid unnecessary model complexity and because improvements were not significant.

The sun glint prediction model introduced in this section is based on solar-sensor geometry and ancillary wind speed. The machine learning and logistic regression analyses underscore the role of VZA under low solar zenith conditions in determining glint probability. Although incorporating observed infrared radiance is expected to improve per-pixel estimates of sun glint intensity, developing and validating such a model was not feasible with geometry-based SeaDAS-derived training data. The prediction model introduced in (6) is therefore expected to perform comparably to SeaDAS's parametrization of Cox and Monk [16]. However, precise modeling and accurate prediction of sun glint in remote sensing data are beyond the scope of this article.

C. Glint Mitigation Using Westward Tilt

Landsat 8/9 OLI nadir-viewing images sense the ground with scan angles up to 7.5° and the VZAs at the swath edge reach 8.3° due to the curvature of the Earth surface [81]. The VZA can exceed 8.3° during off-nadir acquisitions which are typically requested via special collection request (SCR) and granted after evaluation of health and safety of the instrument and spacecraft and their relevance to the mission science requirements.

Given the demonstrated importance of VZA in sun glint probability in earlier sections, we estimated the percentage of sun glint across multiple viewing geometry scenarios. The swath edge VZA values are summarized in Table I and are illustrated schematically in Fig. 9. The first scenario with an FOV of 15° represents the full swath of Landsat 8/9 [82], while scenarios 2–8 use an FOV of 14.4°, corresponding to the design requirement for the Landsat 10 mission concept [2]. The minimum (western) and maximum (eastern) swath edge VZA values were calculated assuming nominal 705-km flight altitude of Landsat 8/9 and Earth's equatorial radius of 6,378 km.

The percentages of sun glint-contaminated pixels for each hypothetical tilt scenario are summarized by SZA intervals in Fig. 10. These statistics were derived by subsetting obser-

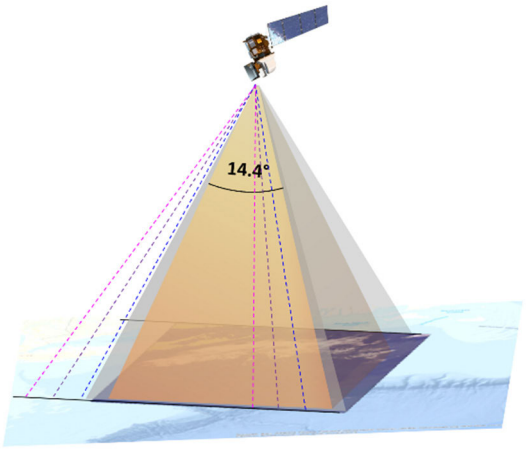


Fig. 9. Schematic of the scan swath for the studied FOV and westward tilt scenarios. The gray and yellow pyramids depict the 15° and 14.4° nadir-viewing cases (Scenarios 1 and 2), respectively. The blue, gray, and magenta dashed lines indicate the FOV = 14.4 with 1°, 2°, and 3° westward tilt configurations (Scenarios 3–5), respectively. Note that angles and distances are not drawn to scale.

TABLE I
SUMMARY OF SWATH EDGE VZA ANGLE VALUES FOR THE ANALYZED WESTWARD TILT SCENARIOS

Scenario	FOV (°)	Tilt (°)	Min VZA (°)	Max VZA (°)
# 1	15	0	-8.3	8.3
# 2	14.4	0	-8.0	8.0
# 3	14.4	1	-9.1	6.9
# 4	14.4	2	-10.2	5.8
# 5	14.4	3	-11.3	4.7
# 6	14.4	6	-14.7	1.3
# 7	14.4	9	-18.0	-2.0
# 8	14.4	12	-21.4	-5.3

vations whose VZA values are within the minimum and maximum ranges corresponding to each hypothetical tilt configuration. As expected for nadir-viewing Landsat data and despite using available off-nadir acquisitions, the number of available observations per scenario (third row in each cell annotation) decreases for extreme tilts configurations. Nevertheless, consistent trends are observed across all scenarios. For each SZA range, the proportion of sun glint contamination decreases progressively as the instrument is further tilted westward, away from the subsolar point. In the three highest glint probability classes in Landsat data ($20° \leq SZA < 25°$, $25° \leq SZA < 30°$, and $30° \leq SZA < 35°$), the percentage of sun glint contaminated pixels is reduced by 11.5%, 21.4%, and 43.8%, respectively, when the nadir-viewing FOV = 14.4° instrument is tilted 3° westward.

D. Mitigation Example

The mitigation analysis demonstrates that even modest across-track westward tilt substantially reduces glint. A 3° westward tilt lowered contamination by 21.3% on average at critical SZA ranges (20°–35°), while larger tilts of 6°–12° progressively reduced contamination by up to 74.1%. A case study during the Landsat 9 underfly of Landsat 8 demonstrated the practical benefit of tilt maneuvers. The Landsat image pairs in Fig. 11 were acquired ~7 min apart on November 17, 2021, during the early commissioning phase of Landsat 9 [83]. Landsat 8 scene center SZA was ~26° at the time of overpass, placing the nadir-viewing imagery near the subsolar point and at high-sun glint risk. Strong sun glint signal is evident across the Landsat 8 true-color image, especially in forward-scattering eastern portion, while the near-simultaneous Landsat 9 image is essentially glint free due to its 14.7° westward roll maneuver. The corresponding VZA and SeaDAS sun glint flags are also shown in Fig. 11, which illustrates the glint contaminated eastern portion of the scene.

Fig. 12 shows the comparison of the spectral response profiles of Landsat 8 and 9 for three regions of interest (ROIs 1–3) shown in the left panels of Fig. 11. The top row presents TOA reflectance for the VSWIR bands, and the bottom row shows atmospherically corrected aquatic reflectance for the Visible and NIR (VNIR) bands from the SeaDAS. The separation between Landsat 8 and Landsat 9 TOA reflectance in the red and infrared spectral bands increases from ROI 1 (low glint in Landsat 8) to ROI 3 (high glint in Landsat 8), indicating the strong contribution of sun glint radiance in nadir-viewing data as function of VZA. In ROI 3, sun glint completely dominates water-leaving radiance and degrades atmospheric correction, resulting in speckle noise manifested as mixed positive/negative spectral profiles in Landsat 8 aquatic reflectance (blue shaded areas represent spectral profiles of individual pixels within the ROI). This example underscores the uncertainty of atmospherically corrected aquatic reflectance in the presence of strong sun glint.

V. DISCUSSION

The reliability of sun glint identification in Landsat 8/9 observations is influenced by limitations in the SeaDAS classification approach. The current SeaDAS threshold of 0.005 at 865 nm is intentionally conservative and may overestimate the number of glint-contaminated pixels [58], [84], [85]. Additional uncertainty arises from the coarse spatial resolution of zonal and meridional wind fields used in Landsat 8/9 provisional Aquatic Reflectance processing, which are interpolated to the Landsat pixel scale for sun glint radiance estimation. This is particularly relevant given that predictor importance analysis identifies wind speed as a major contributing variable. The relatively higher importance of wind speed compared with VZA should be interpreted in the context of Landsat observation geometry, characterized by a relatively narrow FOV and limited sampling at low SZA ($SZA < 20°$) in mid-morning overpass orbit. Under these conditions, the sensitivity of sun glint occurrence to VZA variations is reduced, while wind-driven surface roughness plays a comparatively larger role. Nevertheless, wind speed is not an operationally controllable parameter, whereas viewing geometry can be systematically adjusted and therefore should be prioritized by global survey missions. Moreover, the statistical relationship between sun glint intensity and solar-viewing geometry becomes less robust at finer ground sampling distances of Landsat 8/9 OLI [65], [86]. Despite these limitations, the SeaDAS high sun glint flag remains an applicable and sufficiently conservative benchmark for assessing potential data loss in the absence of mitigation strategies.

Advances in spectral correction methods demonstrate that sun glint-contaminated observations can still yield valid

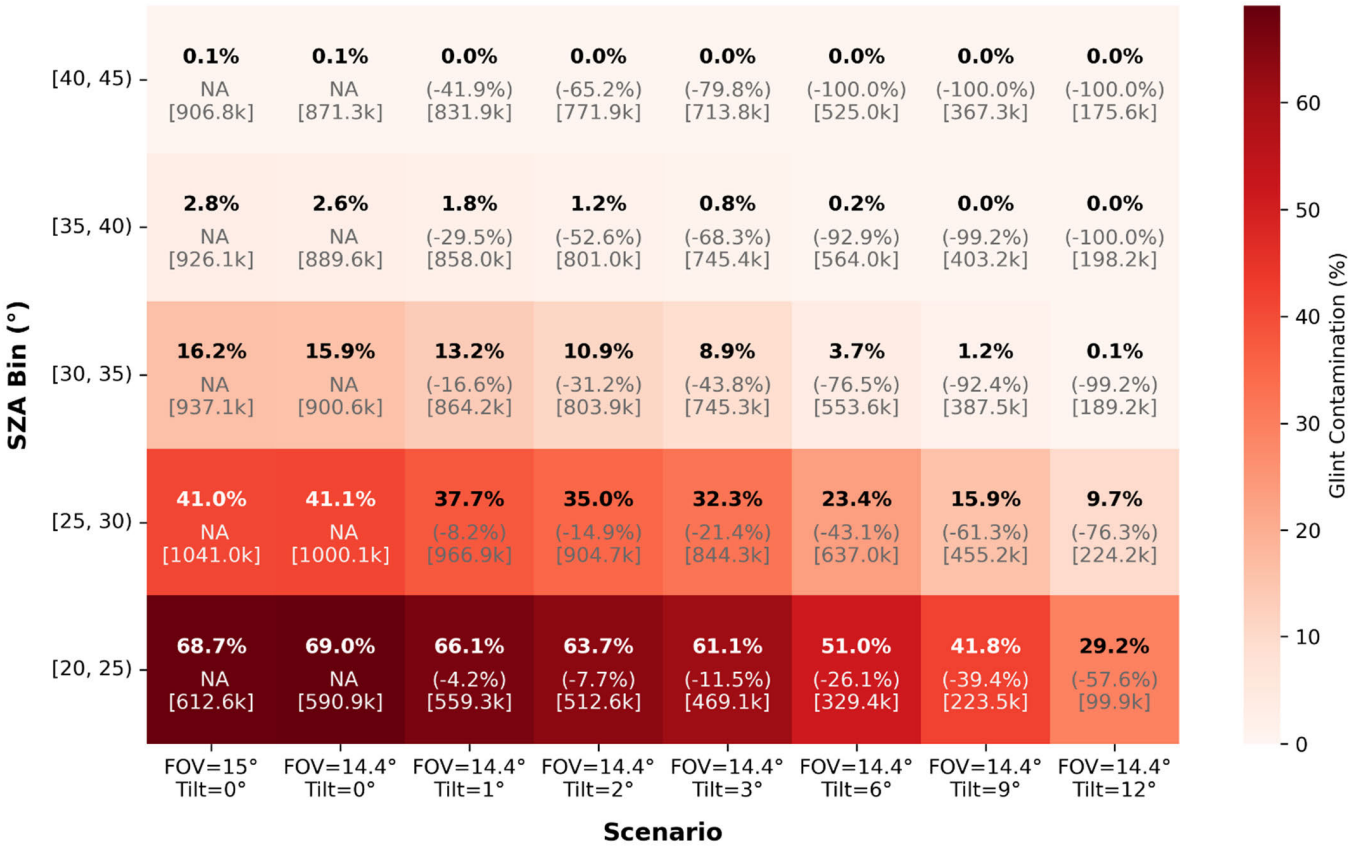


Fig. 10. Ratio of sun glint pixels (percent) across different FOV and westward tilt scenarios (columns) and SZA ranges (rows). Parenthetical values in the second and third lines denote the percentage reduction relative to the nadir-viewing 14.4° FOV (Scenario 2) and the total number of pixels in each scenario/SZA range, respectively.

water-leaving radiance after correction [14], [39], [44], [87]. However, algorithmic correction approaches rely on assumptions regarding spectral behavior, atmospheric conditions, and surface properties that may not hold across all environments. These techniques can estimate and subtract the glint contribution from the observed signal but cannot remove the associated uncertainty and photon shot noise introduced at the measurement stage. As a result, strong glint conditions reduce the effective SNR, and residual errors after correction may still dominate the aquatic signal of interest. For example, the sun glint correction in ACOLITE is optional and disabled by default because the adjacency effects and the presence of haze or cirrus clouds can degrade retrieval accuracy when sun glint is weak or absent [44]. In contrast, observational mitigation strategies, such as modest sensor tilt, are physically straightforward, well understood, and operationally well established. These methods reduce the magnitude of the contaminating signal at acquisition and thereby increase measurement fidelity. Geometry-based assessments of glint risk can further help to identify acquisitions that are more prone to contamination and to guide the selective application of correction algorithms. Although the spatial extent of glint is influenced by surface roughness and wind conditions, first-order glint risk can be effectively estimated from viewing and illumination geometry alone. Therefore, observational mitigation and post-acquisition algorithmic correction should be viewed as complementary approaches. Reducing sun glint at the source increases SNR and the effectiveness of subsequent correction methods, ultimately supporting higher quality aquatic observations.

Evaluating tilt-based mitigation strategies requires careful consideration of impacts on terrestrial observation requirements. Westward tilting increases the viewing angle on the western edge of the swath, which may be acceptable for an OLI-like instrument with narrow to moderate FOV but could amplify bidirectional reflectance distribution function (BRDF) effects over land for instruments with broad FOV. Wide-angle instruments are particularly susceptible to anisotropic reflectance that must be addressed via BRDF correction to avoid radiometric bias [88]. Tilting away from the subsolar region may also influence cloud contamination patterns by modifying the projection of clouds and the distribution of their cast shadows in the image. These considerations highlight the need to balance the aquatic and terrestrial requirements when designing operational tilt strategies.

Despite the above limitations and tradeoffs, our results reveal clear and actionable patterns. Analysis of Landsat 8 and 9 observations demonstrates that under comparable wind conditions, sun-sensor geometry is the dominant driver for sun glint contamination. This result has direct implications for any future remote sensing mission that includes aquatic VSWIR observations, particularly as terrestrial missions are increasingly expected to support aquatic science. Quantitative analyses presented here underscore how incorporating tilt maneuvers in future mission designs could increase the quality

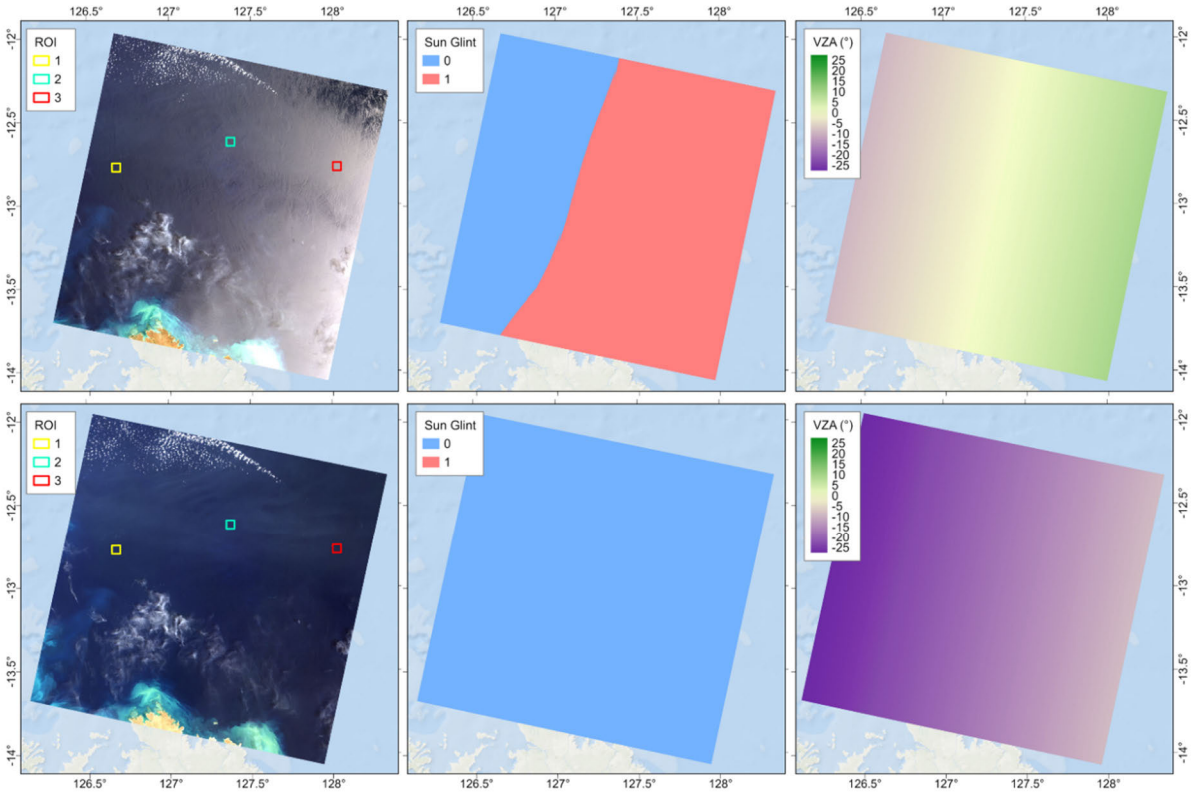


Fig. 11. Example of sun glint in a nadir-viewing Landsat 8 acquisition (top row) and a near-simultaneous glint-free off-nadir Landsat 9 observation (bottom row) on November 17, 2021, over WRS-2 Path 108/Row 69 along the northern coast of Australia. (Left column) Level-1 TOA reflectance (true-color RGB) displayed with identical stretch functions, middle column: sun glint classification from SeaDAS, and right column: per-pixel VZA, degrees).

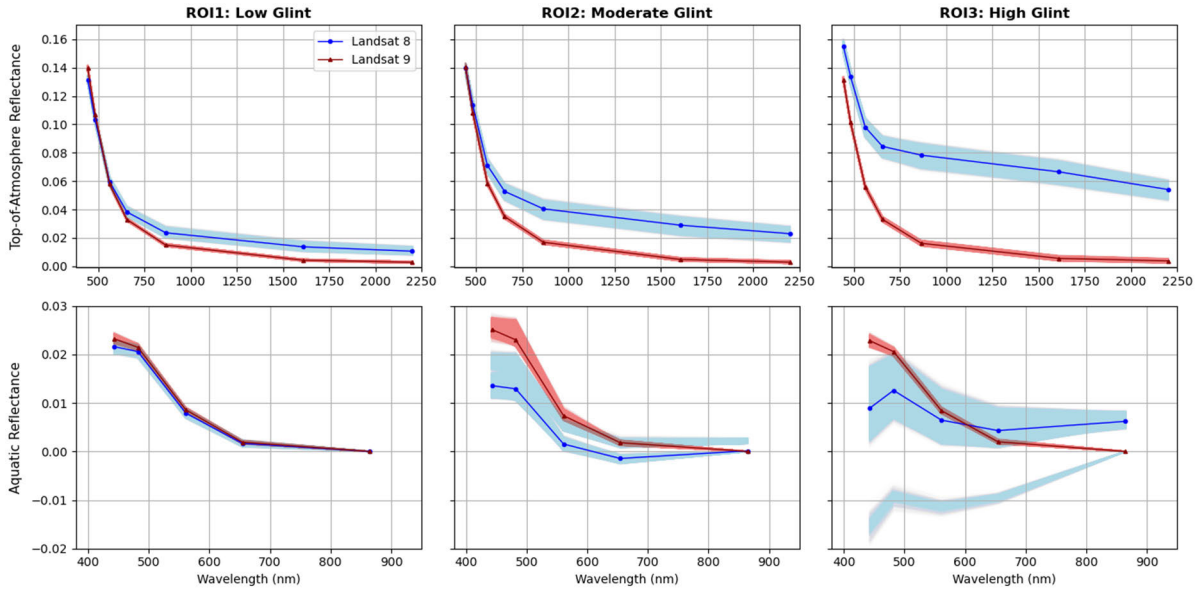


Fig. 12. Spectral profiles from 0.05° × 0.05° (~ 5.5 × 5.5 km) regions of interests in Landsat 8 and 9 images. The top row shows TOA reflectance in the VSWIR wavelength range, and the bottom row shows aquatic reflectance in the VNIR range. Columns from left to right correspond to low, medium, and high-sun glint intensity in nadir-viewing Landsat 8 data. The blue and red shaded regions represent the spectral profiles of ~33 000 individual Landsat 8/9 pixels within each ROI, with the mean profile shown as dark blue/red lines. (Bottom left) Under low-sun glint conditions, Landsat 8 and 9 provide comparable aquatic reflectance values; however, in the presence of sun glint (bottom center and bottom right), aquatic reflectance from nadir-viewing Landsat 8 becomes highly uncertain. The large spread in reflectance values in shorter wavelengths and bimodal distribution observed in some spectral bands are driven by water-surface roughness and sensitivity of atmospheric correction to the orientation of wave facets.

and utility of collected data. Without a mitigation strategy, missions risk losing quality aquatic data in approximately 40% of acquisitions at low to mid-latitudes (SZA < 35°). This problem is exacerbated by persistent cloud cover in

those regions, further limiting data availability. An observation concept that adopts glint-mitigation tilt strategies combined with robust post-acquisition detection and correction methods is therefore essential to maximize the aquatic data quality.

Some upcoming missions illustrate how these findings intersect with emerging design choices. For instance, the surface biology and geology (SBG)-VSWIR was considering a permanent 3°–5° westward tilt to reduce sun glint [89], [90], [91], in combination with spectral correction approaches for coastal regions [36]. Landsat 10 will use a long-term acquisition plan (LTAP) to systematically image the land masses, inland water bodies, near-shore coastal zones, and reefs [92]. While off-nadir imaging capability is planned, a fixed systematic tilting is not part of the current imaging concept for the next Landsat mission.

The choice between along-track and across-track tilt configurations to avoid sun glint depends on instrument architecture, swath geometry, and mission objectives. An across-track tilt is generally more suitable for push-broom sensors (e.g., Sentinel-3 OLCI), where fixed viewing geometry enables continuous imaging without mechanical motion. In contrast, along-track tilt is operationally more compatible with whiskbroom radiometers using rotating scan mirrors (e.g., SeaWiFS and PACE OCI) [50], [58], [93]. Along-track configurations typically require at least two tilt maneuvers per orbit, which can increase operational complexity and impose mechanical stress, particularly for instruments not designed for frequent repointing [94]. These maneuvers may also interrupt nominal image acquisition, leading to potential data gaps during transitions. As a result, along-track tilting is better suited for missions with large FOV and swath widths or for tasked acquisition strategies, where coverage continuity is not impacted or is less critical. For global survey missions with relatively narrow FOV, such as Landsat 8 and 9, a fixed across-track tilt is less disruptive to routine imaging operations and helps to preserve the consistent revisit coverage. Regardless of the configuration, the tilt direction should be oriented away from the subsolar point. For the across-track tilt in a sun-synchronous mission, this corresponds to a westward tilt for morning overpass orbits (e.g., Landsat 8/9) and an eastward tilt for afternoon overpass missions.

The need for glint mitigation is strongly dependent on latitude and the season. Analysis of Landsat 8 and 9 data showed that sun glint is rare for SZA > 40° and generally negligible for SZA > 35°. Thus, glint occurrence is largely confined to within ~60° latitude of the subsolar point (e.g., 30°S–30°N near spring/fall equinox, or 5°S–55°N during northern hemisphere summer solstice), with the highest intensity near the center of this latitudinal belt. These patterns indicate that adaptive tilt schedules, where tilt gradually increases as SZA decreases toward the subsolar point and returns to nadir viewing at higher SZAs could provide an efficient strategy to minimize glint while moderating impacts on terrestrial observations. Incorporating geometric-based glint screening or real-time glint probability metrics into onboard acquisition planning could also help to prioritize acquisitions and optimize downlink usage, particularly for imaging spectroscopy missions with a medium-fine ground sampling distance that acquire large data volumes. Such approaches could enable the prioritization of high value, glint-free observations to increase overall data return for aquatic science applications.

VI. Conclusion

This study evaluated the sun glint issue in optical Earth-observing missions and examined the westward tilt concept for mitigation following a data-driven approach. Analysis of Landsat 8 and 9 data confirmed that the SZA and wind speed are the primary factors controlling sun glint, with VZA further influencing susceptibility for sun-synchronous missions. Adoption of a modest westward tilt away from the subsolar point substantially reduced the sun glint in tropical and subtropical regions, with larger tilts yielding progressively stronger mitigation. Integrating a fixed or adaptive westward tilt acquisition-based mitigation, together with post-acquisition glint correction, offers a practical approach to improve aquatic remote sensing, particularly in low-latitude regions where high-quality observations are most needed, while maintaining continuity for terrestrial applications.

Acknowledgment

The authors gratefully acknowledge Dr. Nima Pahlevan for his invaluable contributions in conceptualizing and formalizing the methodology during his 2018–2023 Landsat Science Team tenure. They also thank Keith Loftin and Sakib Kabir for their valuable feedback and insightful discussions. The contributions by KBR and ESTS were conducted through USGS Contract Number 140G0121D001 under the EROS Technical Support Services Contract. Any use of trade, firm, or product names is for descriptive purposes only and does not imply endorsement by the U.S. Government.

References

[1] M. A. Wulder et al., "Fifty years of Landsat science and impacts," *Remote Sens. Environ.*, vol. 280, Oct. 2022, Art. no. 113195, doi: 10.1016/j.rse.2022.113195.

[2] D. P. Roy et al., "The next Landsat: Mission turning point?" *Remote Sens. Environ.*, vol. 332, Jan. 2026, Art. no. 115087, doi: 10.1016/j.rse.2025.115087.

[3] J. R. Irons and J. L. Dwyer, "An overview of the Landsat data continuity mission," *Proc. SPIE*, vol. 7695, pp. 58–64, May 2010, doi: 10.1117/12.850416.

[4] N. Pahlevan, Z. Lee, J. Wei, C. B. Schaaf, J. R. Schott, and A. Berk, "On-orbit radiometric characterization of OLI (Landsat-8) for applications in aquatic remote sensing," *Remote Sens. Environ.*, vol. 154, pp. 272–284, Nov. 2014, doi: 10.1016/j.rse.2014.08.001.

[5] S. Kabir, N. Pahlevan, R. E. O'Shea, and B. B. Barnes, "Leveraging Landsat-8/-9 underfly observations to evaluate consistency in reflectance products over aquatic environments," *Remote Sens. Environ.*, vol. 296, Oct. 2023, Art. no. 113755, doi: 10.1016/j.rse.2023.113755.

[6] N. Pahlevan et al., "Landsat 8 remote sensing reflectance (RRS) products: Evaluations, intercomparisons, and enhancements," *Remote Sens. Environ.*, vol. 190, pp. 289–301, Mar. 2017, doi: 10.1016/j.rse.2016.12.030.

[7] N. Pahlevan et al., "ACIX-Aqua: A global assessment of atmospheric correction methods for Landsat-8 and Sentinel-2 over lakes, rivers, and coastal waters," *Remote Sens. Environ.*, vol. 258, Jun. 2021, Art. no. 112366, doi: 10.1016/j.rse.2021.112366.

[8] C. J. Crawford et al., "The 50-year Landsat collection 2 archive," *Sci. Remote Sens.*, vol. 8, Dec. 2023, Art. no. 100103, doi: 10.1016/j.srs.2023.100103.

[9] A. Pacheco, J. Horta, C. Loureiro, and Ó. Ferreira, "Retrieval of nearshore bathymetry from Landsat 8 images: A tool for coastal monitoring in shallow waters," *Remote Sens. Environ.*, vol. 159, pp. 102–116, Mar. 2015, doi: 10.1016/j.rse.2014.12.004.

[10] D. Keith et al., "Monitoring algal blooms in drinking water reservoirs using the Landsat-8 operational land imager," *Int. J. Remote Sens.*, vol. 39, no. 9, pp. 2818–2846, May 2018, doi: 10.1080/01431161.2018.1430912.

[11] C. Kuhn et al., "Performance of Landsat-8 and Sentinel-2 surface reflectance products for river remote sensing retrievals of chlorophyll–A and turbidity," *Remote Sens. Environ.*, vol. 224, pp. 104–118, Apr. 2019, doi: 10.1016/j.rse.2019.01.023.

[12] F. Steinmetz, P.-Y. Deschamps, and D. Ramon, "Atmospheric correction in presence of sun glint: Application to MERIS," *Opt. Exp.*, vol. 19, no. 10, pp. 9783–9800, 2011, doi: 10.1364/oe.19.009783.

[13] B. T. Overstreet and C. J. Legleiter, "Removing sun glint from optical remote sensing images of shallow rivers," *Earth Surf. Processes Landforms*, vol. 42, no. 2, pp. 318–333, Feb. 2017, doi: 10.1002/esp.4063.

[14] T. Harmel, M. Chami, T. Tormos, N. Reynaud, and P.-A. Danis, "Sunglint correction of the multi-spectral instrument (MSI)-SENTINEL-2 imagery over inland and sea waters from SWIR bands," *Remote Sens. Environ.*, vol. 204, pp. 308–321, Jan. 2018, doi: 10.1016/j.rse.2017.10.022.

[15] F. E. Müller-Karger et al., "Satellite sensor requirements for monitoring essential biodiversity variables of coastal ecosystems," *Ecol. Appl.*, vol. 28, no. 3, pp. 749–760, Apr. 2018, doi: 10.1002/eap.1682.

[16] C. Cox and W. Munk, "Measurement of the roughness of the sea surface from photographs of the sun's glitter," *J. Opt. Soc. Amer.*, vol. 44, no. 11, pp. 838–850, 1954, doi: 10.1364/JOSA.44.000838.

[17] *Engineering, and Medicine, Thriving on Our Changing Planet: A Decadal Strategy for Earth Observation From Space*, National Academies of Sciences, Washington, DC, USA, 2019, doi: 10.17226/24938.

[18] Z. Wu et al., "User needs for future Landsat missions," *Remote Sens. Environ.*, vol. 231, Sep. 2019, Art. no. 111214, doi: 10.1016/j.rse.2019.111214.

[19] P. L. Brezonik, L. G. Olmanson, J. C. Finlay, and M. E. Bauer, "Factors affecting the measurement of CDOM by remote sensing of optically complex inland waters," *Remote Sens. Environ.*, vol. 157, pp. 199–215, Feb. 2015, doi: 10.1016/j.rse.2014.04.033.

[20] L. G. Olmanson, P. L. Brezonik, J. C. Finlay, and M. E. Bauer, "Comparison of Landsat 8 and Landsat 7 for regional measurements of CDOM and water clarity in lakes," *Remote Sens. Environ.*, vol. 185, pp. 119–128, Nov. 2016, doi: 10.1016/j.rse.2016.01.007.

[21] L. G. Olmanson et al., "Regional measurements and spatial/temporal analysis of CDOM in 10,000 + optically variable Minnesota lakes using Landsat 8 imagery," *Sci. Total Environ.*, vol. 724, Jul. 2020, Art. no. 138141, doi: 10.1016/j.scitotenv.2020.138141.

[22] M. Babin and D. Stramski, "Variations in the mass-specific absorption coefficient of mineral particles suspended in water," *Limnology Oceanogr.*, vol. 49, no. 3, pp. 756–767, May 2004, doi: 10.4319/lo.2004.49.3.0756.

[23] R. M. Diehl, K. L. Underwood, R. Watt, S. D. Hamshaw, and N. Pahlevan, "Evaluating opportunities for broad-scale remote sensing of total suspended solids on small rivers," *Remote Sens. Appl., Soc. Environ.*, vol. 35, Aug. 2024, Art. no. 101234, doi: 10.1016/j.rsase.2024.101234.

[24] N. Pahlevan et al., "Seamless retrievals of chlorophyll—A from Sentinel-2 (MSI) and Sentinel-3 (OLCI) in inland and coastal waters: A machine-learning approach," *Remote Sens. Environ.*, vol. 240, Apr. 2020, Art. no. 111604, doi: 10.1016/j.rse.2019.111604.

[25] N. Pahlevan et al., "Simultaneous retrieval of selected optical water quality indicators from Landsat-8, Sentinel-2, and Sentinel-3," *Remote Sens. Environ.*, vol. 270, Mar. 2022, Art. no. 112860, doi: 10.1016/j.rse.2021.112860.

[26] J. C. Ho, A. M. Michalak, and N. Pahlevan, "Widespread global increase in intense lake phytoplankton Blooms since the 1980s," *Nature*, vol. 574, no. 7780, pp. 667–670, Oct. 2019, doi: 10.1038/s41586-019-1648-7.

[27] R. P. Stumpf et al., "Challenges for mapping cyanotoxin patterns from remote sensing of cyanobacteria," *Harmful Algae*, vol. 54, pp. 160–173, Apr. 2016, doi: 10.1016/j.hal.2016.01.005.

[28] E. A. Urquhart, B. A. Schaeffer, R. P. Stumpf, K. A. Loftin, and P. J. Werdell, "A method for examining temporal changes in cyanobacterial harmful algal Bloom spatial extent using satellite remote sensing," *Harmful Algae*, vol. 67, pp. 144–152, Jul. 2017, doi: 10.1016/j.hal.2017.06.001.

[29] J. M. Clark et al., "Satellite monitoring of cyanobacterial harmful algal Bloom frequency in recreational waters and drinking water sources," *Ecological Indicators*, vol. 80, pp. 84–95, Sep. 2017, doi: 10.1016/j.ecolind.2017.04.046.

[30] S. Mishra, R. P. Stumpf, B. A. Schaeffer, P. J. Werdell, K. A. Loftin, and A. Meredith, "Measurement of cyanobacterial Bloom magnitude using satellite remote sensing," *Sci. Rep.*, vol. 9, no. 1, p. 18310, Dec. 2019, doi: 10.1038/s41598-019-54453-y.

[31] B. A. Schaeffer et al., "Satellites quantify the spatial extent of cyanobacterial blooms across the United States at multiple scales," *Ecol. Indicators*, vol. 140, Jul. 2022, Art. no. 108990, doi: 10.1016/j.ecolind.2022.108990.

[32] R. E. O'Shea et al., "Advancing cyanobacteria biomass estimation from hyperspectral observations: Demonstrations with HICO and PRISMA imagery," *Remote Sens. Environ.*, vol. 266, Dec. 2021, Art. no. 112693, doi: 10.1016/j.rse.2021.112693.

[33] K. Zolfaghari et al., "Impact of spectral resolution on quantifying cyanobacteria in lakes and reservoirs: A machine-learning assessment," *IEEE Trans. Geosci. Remote Sens.*, vol. 60, 2022, Art. no. 5515520, doi: 10.1109/TGRS.2021.3114635.

[34] G. Kirches, C. Brockmann, R. Preusker, P. Gamba, and O. Hagolle. (Jun. 2024). *Sentinel-2 Next Generation Phase 0 Scientific Support Study*. Accessed: Apr. 9, 2026. [Online]. Available: https://esamultimedia.esa.int/docs/EarthObservation/S2NG_Phase_0_Science_Support_Study_Final_Report.pdf

[35] K. Cawse-Nicholson et al., "NASA's surface biology and geology designated observable: A perspective on surface imaging algorithms," *Remote Sens. Environ.*, vol. 257, May 2021, Art. no. 112349, doi: 10.1016/j.rse.2021.112349.

[36] E. Greenberg et al., "An improved scheme for correcting remote spectral surface reflectance simultaneously for terrestrial BRDF and water-surface sunglint in coastal environments," *J. Geophys. Res., Biogeosciences*, vol. 127, no. 3, p. 2021, Mar. 2022, doi: 10.1029/2021jg006712.

[37] H. R. Gordon and M. Wang, "Surface-roughness considerations for atmospheric correction of ocean color sensors 1: The Rayleigh-scattering component," *Appl. Opt.*, vol. 31, no. 21, pp. 4247–4260, 1992, doi: 10.1364/ao.31.004247.

[38] H. R. Gordon, "Atmospheric correction of ocean color imagery in the Earth Observing System era," *J. Geophys. Res., Atmos.*, vol. 102, no. D14, pp. 17081–17106, Jul. 1997, doi: 10.1029/96jd02443.

[39] P. Gege, "WASI-2D: A software tool for regionally optimized analysis of imaging spectrometer data from deep and shallow waters," *Comput. Geosci.*, vol. 62, pp. 208–215, Jan. 2014, doi: 10.1016/j.cageo.2013.07.022.

[40] H. Zhang and M. Wang, "Evaluation of sun glint models using MODIS measurements," *J. Quant. Spectrosc. Radiat. Transf.*, vol. 111, no. 3, pp. 492–506, Feb. 2010, doi: 10.1016/j.jqsrt.2009.10.001.

[41] C. D. Mobley, J. Werdell, B. Franz, Z. Ahmad, and S. Bailey. (2016). *Atmospheric Correction for Satellite Ocean Color Radiometry*. Accessed: Dec. 10, 2025. [Online]. Available: https://ntrs.nasa.gov/citations/20160011399

[42] D. Müller et al., "The ocean colour climate change initiative: II. spatial and temporal homogeneity of satellite data retrieval due to systematic effects in atmospheric correction processors," *Remote Sens. Environ.*, vol. 162, pp. 257–270, Jun. 2015, doi: 10.1016/j.rse.2015.01.033.

[43] L. He, J. M. Chen, and K.-S. Chen, "Simulation and SMAP observation of sun-glint over the land surface at the L-band," *IEEE Trans. Geosci. Remote Sens.*, vol. 55, no. 5, pp. 2589–2604, May 2017, doi: 10.1109/TGRS.2017.2648502.

[44] Q. Vanhellemont, "Adaptation of the dark spectrum fitting atmospheric correction for aquatic applications of the Landsat and Sentinel-2 archives," *Remote Sens. Environ.*, vol. 225, pp. 175–192, May 2019, doi: 10.1016/j.rse.2019.03.010.

[45] D. R. Mishra et al., "Decline in phytoplankton biomass along Indian coastal waters due to COVID-19 lockdown," *Remote Sens.*, vol. 12, no. 16, p. 2584, Aug. 2020, doi: 10.3390/rs12162584.

[46] N. K. Hannadige et al., "Atmospheric correction over the ocean for hyperspectral radiometers using multi-angle polarimetric retrievals," *Opt. Exp.*, vol. 29, no. 3, pp. 4504–4522, 2021, doi: 10.1364/oe.408467.

[47] J. He, G. Christakos, J. Wu, M. Li, and J. Leng, "Spatiotemporal BME characterization and mapping of sea surface chlorophyll in Chesapeake bay (USA) using auxiliary sea surface temperature data," *Sci. Total Environ.*, vol. 794, Nov. 2021, Art. no. 148670, doi: 10.1016/j.scitotenv.2021.148670.

[48] M. Werther et al., "A Bayesian approach for remote sensing of chlorophyll—A and associated retrieval uncertainty in oligotrophic and mesotrophic lakes," *Remote Sens. Environ.*, vol. 283, Dec. 2022, Art. no. 113295, doi: 10.1016/j.rse.2022.113295.

[49] S. B. Hooker and E. R. Firestone. (1992). *SeaWiFS Technical Report Series: Volume 1: An Overview of SeaWiFS and Ocean Color*. Accessed: Dec. 10, 2025. [Online]. Available: https://oceancolor.gsfc.nasa.gov/docs/technical/seawifs_reports/prelaunch/PreLVol1.pdf

[50] E. T. Gorman, D. A. Kubalak, D. Patel, D. B. Mott, G. Meister, and P. J. Werdell, "The NASA plankton, aerosol, cloud, ocean ecosystem (PACE) mission: An emerging era of global, hyperspectral Earth system remote sensing," *Proc. SPIE*, vol. 11151, pp. 78–84, Oct. 2019, doi: 10.1117/12.2537146.

[51] J. Nieke et al., "The Ocean and Land Colour Imager (OLCI) for the Sentinel 3 GMES Mission: Status and first test results," *Proc. SPIE*, vol. 8528, pp. 49–57, Nov. 2012, doi: 10.1117/12.977247.

[52] S. B. Hooker, E. R. Firestone, and W. W. Gregg. (1992). *Seawifs Technical Report Series*. Volume 2: Analysis of Orbit Selection for Seawifs: Ascending Versus Descending Node. Accessed: Dec. 10, 2025. [Online]. Available: https://ntrs.nasa.gov/citations/19930019308

[53] M. Wang and S. W. Bailey, "Correction of sun glint contamination on the SeaWiFS ocean and atmosphere products," *Appl. Opt.*, vol. 40, no. 27, pp. 4790–4798, 2001, doi: 10.1364/ao.40.004790.

[54] J. D. Hedley, A. R. Harborne, and P. J. Mumby, "Technical note: Simple and robust removal of sun glint for mapping shallow-water benthos," *Int. J. Remote Sens.*, vol. 26, no. 10, pp. 2107–2112, May 2005, doi: 10.1080/01431160500034086.

[55] B.-C. Gao and R.-R. Li, "Correction of sunglint effects in high spatial resolution hyperspectral imagery using SWIR or NIR bands and taking account of spectral variation of refractive index of water," *Adv. Environ. Eng. Res.*, vol. 2, no. 3, pp. 1–15, 2021, doi: 10.21926/aeer.2103017.

[56] C. D. Mobley, *Light and Water: Radiative Transfer in Natural Waters*. New York, NY, USA: Academic, 1994.

[57] E. J. Hochberg, S. Andrefouet, and M. R. Tyler, "Sea surface correction of high spatial resolution ikonos images to improve bottom mapping in near-shore environments," *IEEE Trans. Geosci. Remote Sens.*, vol. 41, no. 7, pp. 1724–1729, Jul. 2003, doi: 10.1109/TGRS.2003.815408.

[58] S. Kay, J. D. Hedley, and S. Lavender, "Sun glint correction of high and low spatial resolution images of aquatic scenes: A review of methods for visible and near-infrared wavelengths," *Remote Sens.*, vol. 1, no. 4, pp. 697–730, Oct. 2009, doi: 10.3390/rs1040697.

[59] S. Kay, J. Hedley, and S. Lavender, "Sun glint estimation in marine satellite images: A comparison of results from calculation and radiative transfer modeling," *Appl. Opt.*, vol. 52, no. 23, pp. 5631–5639, 2013, doi: 10.1364/ao.52.005631.

[60] P. Gege and P. Grötsch, "A spectral model for correcting sun glint and sky glint," *Proc. SPIE*, vol. 2016, pp. 1–10, Oct. 2016.

[61] N. Bohn et al., "Simultaneous modeling of water-leaving reflectance and sun and sky glint contributions from imaging spectroscopy measurements," *Appl. Opt.*, vol. 64, no. 30, pp. 9094–9105, 2025, doi: 10.1364/ao.569763.

[62] *Landsat 8-9 Operational Land Imager/Thermal Infrared Sensor Level-2 Provisional Aquatic Reflectance, Collection 2, Earth Resources Observation and Science* (EROS) Center, Sioux Falls, SD, USA, 2020.

[63] B. Page, C. J. Crawford, S. Arab, G. Schmidt, C. Barnes, and D. Wellington, "Origins, evolutions, and future directions of Landsat science products for advancing global inland water and coastal ocean observations," *Earth Syst. Sci. Data*, vol. 18, no. 2, pp. 779–800, Feb. 2026, doi: 10.5194/essd-18-779-2026.

[64] *Landsat 8-9 Operational Land Imager/Thermal Infrared Sensor Level-1, Collection 2, Earth Resources Observation and Science (EROS) Center*, Sioux Falls, SD, USA, 2020, doi: 10.5066/P975CC9B.

[65] B. A. Franz, S. W. Bailey, N. Kuring, and P. J. Werdell, "Ocean color measurements with the operational land imager on Landsat-8: Implementation and evaluation in SeaDAS," *J. Appl. Remote Sens.*, vol. 9, no. 1, Mar. 2015, Art. no. 096070, doi: 10.1117/1.jrs.9.096070.

[66] M. M. Rienecker et al. (2008). *The GEOS-5 Data Assimilation System-Documentation of Versions 5.0*. 1, 5.1. 0, and 5.2. 0. Accessed: Dec. 10, 2025. [Online]. Available: https://ntrs.nasa.gov/citations/20120011955

[67] S. B. Hooker et al. (1995). SeaWiFS Technical Report Series., Volume 28: *SeaWiFS Algorithms*, Part 1. Accessed: Dec. 10, 2025. [Online]. Available: https://ntrs.nasa.gov/citations/19950025429

[68] Z. Zhu, S. Wang, and C. E. Woodcock, "Improvement and expansion of the fmask algorithm: Cloud, cloud shadow, and snow detection for Landsats 4–7, 8, and Sentinel 2 images," *Remote Sens. Environ.*, vol. 159, pp. 269–277, Mar. 2015, doi: 10.1016/j.rse.2014.12.014.

[69] F. M. Bréon and N. Henriot, "Spaceborne observations of ocean glint reflectance and modeling of wave slope distributions," *J. Geophys. Research: Oceans*, vol. 111, no. C6, p. 2005, Jun. 2006, doi: 10.1029/2005jc003343.

[70] H. K. Zhang, D. P. Roy, and V. Kovalskyy, "Optimal solar geometry definition for global long-term Landsat time-series bidirectional reflectance normalization," *IEEE Trans. Geosci. Remote Sens.*, vol. 54, no. 3, pp. 1410–1418, Mar. 2016, doi: 10.1109/TGRS.2015.2480684.

[71] C. D. Mobley, "Estimation of the remote-sensing reflectance from above-surface measurements," *Appl. Opt.*, vol. 38, no. 36, pp. 7442–7455, 1999, doi: 10.1364/ao.38.007442.

[72] Z. Wang and M. Costa, "Autonomous shipborne in situ reflectance data in optically complex coastal waters: A case study of the salish sea, Canada," *Frontiers Remote Sens.*, vol. 3, 2022, Art. no. 867570, doi: 10.3389/frsen.2022.867570.

[73] T. Chen and C. Guestrin, "XGBoost: A scalable tree boosting system," in *Proc. 22nd ACM SIGKDD Int. Conf. Knowl. Discovery Data Mining*, Aug. 2016, pp. 785–794, doi: 10.1145/2939672.2939785.

[74] M. Belgiu and L. Drăguţ, "Random forest in remote sensing: A review of applications and future directions," *ISPRS J. Photogramm. Remote Sens.*, vol. 114, pp. 24–31, Apr. 2016, doi: 10.1016/j.isprsjprs.2016.01.011.

[75] A. E. Maxwell, T. A. Warner, and F. Fang, "Implementation of machine-learning classification in remote sensing: An applied review," *Int. J. Remote Sens.*, vol. 39, no. 9, pp. 2784–2817, May 2018, doi: 10.1080/01431161.2018.1433343.

[76] S. Lundberg and S.-I. Lee, "A unified approach to interpreting model predictions," 2017, *arXiv:1705.07874*.

[77] R. Couronné, P. Probst, and A.-L. Boulesteix, "Random forest versus logistic regression: A large-scale benchmark experiment," *BMC Bioinf.*, vol. 19, no. 1, p. 270, Dec. 2018, doi: 10.1186/s12859-018-2264-5.

[78] S. Menard, "Standards for standardized logistic regression coefficients," *Social Forces*, vol. 89, no. 4, pp. 1409–1428, Jun. 2011, doi: 10.1093/sf/89.4.1409.

[79] G. Montavon, G. Orr, and K.-R. Müller, *Neural Networks: Tricks of the Trade*. Cham, Switzerland: Springer, 2012.

[80] P. De Vis, F. Mélin, S. E. Hunt, R. Morrone, M. Sinclair, and B. Bell, "Ancillary data uncertainties within the SeaDAS uncertainty budget for ocean colour retrievals," *Remote Sens.*, vol. 14, no. 3, p. 497, Jan. 2022, doi: 10.3390/rs14030497.

[81] J. Ju et al., "The harmonized Landsat and Sentinel-2 version 2.0 surface reflectance dataset," *Remote Sens. Environ.*, vol. 324, Jul. 2025, Art. no. 114723, doi: 10.1016/j.rse.2025.114723.

[82] J. G. Masek et al., "Landsat 9: Empowering open science and applications through continuity," *Remote Sens. Environ.*, vol. 248, Oct. 2020, Art. no. 111968.

[83] E. Kaita et al., "Landsat 9 cross calibration under-fly of Landsat 8: Planning, and execution," *Remote Sens.*, vol. 14, no. 21, p. 5414, Oct. 2022, doi: 10.3390/rs14215414.

[84] R. K. Singh and P. Shanmugam, "A robust method for removal of glint effects from satellite ocean colour imagery," *Ocean Sci. Discuss.*, vol. 11, no. 6, pp. 2791–2829, 2014, doi: 10.5194/osd-11-2791-2014.

[85] A. Pisano, F. Bignami, and R. Santoleri, "Oil spill detection in glint-contaminated near-infrared MODIS imagery," *Remote Sens.*, vol. 7, no. 1, pp. 1112–1134, Jan. 2015, doi: 10.3390/rs70101112.

[86] E. J. Hochberg et al. (2011). HyspIRI Sunglint Subgroup Report. [Online]. Available: https://www.researchgate.net/publication/259827816_Summary_of_HyspIRI_Sunglint_Subgroup_Discussions_and_Analyses_Fall_2009_-_Spring_2010

[87] Q. Xing and C. Hu, "Mapping macroalgal blooms in the Yellow Sea and East China Sea using HJ-1 and Landsat data: Application of a virtual baseline reflectance height technique," *Remote Sens. Environ.*, vol. 178, pp. 113–126, Jun. 2016, doi: 10.1016/j.rse.2016.02.065.

[88] M. Claverie et al., "Evaluation of medium spatial resolution BRDF-adjustment techniques using multi-angular SPOT4 (Take5) acquisitions," *Remote Sens.*, vol. 7, no. 9, pp. 12057–12075, Sep. 2015, doi: 10.3390/rs70912057.

[89] R. O. Green et al., "Surface biology and geology (SBG) visible to short wavelength infrared (VSWIR) wide swath instrument concept," in *Proc. IEEE Aerosp. Conf. (AERO)*, Mar. 2022, pp. 1–10, doi: 10.1109/AERO53065.2022.9843676.

[90] H. M. Dierssen et al., "Synergies between NASA's hyperspectral aquatic missions PACE, GLIMR, and SBG: Opportunities for new science and applications," *J. Geophys. Res., Biogeosciences*, vol. 128, no. 10, p. 2023, Oct. 2023, doi: 10.1029/2023jg007574.

[91] R. Eckert, C. Ade, D. R. Thompson, K. Cawse-Nicholson, U. N. Bohn, and P. G. Brodrick, "SBG 2024 TIM meeting summary: Current progress and future goals of the SBG mission," ORNL Distrib. Act. Arch. Center, Oak Ridge, TN, USA, Tech. Rep. SBG_TIM_2024_Report_2433, Jun. 2025, doi: 10.3334/ORNLDAAC/2433.

[92] C. J. Crawford, S. Arab, K. Alberts, B. T. Chinn, A. J. Crenshaw, and L. M. Tornabene, "The Landsat 8/9 long term acquisition plan for Earth's continental landmasses and near-shore coastal zones, version 1.0," U.S. Geological Surv. Data Release, Sioux Falls, SD, USA, 2025, doi: 10.5066/P1WXQ2JN.

[93] J. Nieke et al., "Ocean and land color imager on Sentinel-3," in *Optical Payloads for Space Missions*. Hoboken, NJ, USA: Wiley, 2015, pp. 223–245, doi: 10.1002/9781118945179.ch10.

[94] S. Petro, K. Pham, and G. Hilton, "Plankton, aerosol, cloud, ocean ecosystem (PACE) mission integration and testing," in *Proc. IEEE Aerosp. Conf.*, Mar. 2020, pp. 1–20, doi: 10.1109/AERO47225.2020.9172326.